Article

Investigation of Non-Uniform Inflow Effects on Impeller Forces in Axial-Flow Pumps Operating as Turbines

Kan Kan [1,2,*], Qingying Zhang [1], Hui Xu [2,3], Jiangang Feng [2,3], Zhenguo Song [4], Jianping Cheng [4] and Maxime Binama [5]

1 School of Electrical and Power Engineering, Hohai University, Nanjing 211100, China; 211306020020@hhu.edu.cn
2 College of Water Conservancy and Hydropower Engineering, Hohai University, Nanjing 210098, China; hxu@hhu.edu.cn (H.X.); jgfeng@hhu.edu.cn (J.F.)
3 College of Agricultural Science and Engineering, Hohai University, Nanjing 211100, China
4 China Ship Development and Design Center, Wuhan 430064, China; whsmxt2020042@163.com (Z.S.); whsmdl2019042@163.com (J.C.)
5 College of Science and Technology (MEE Department), University of Rwanda, Kigali 3900, Rwanda; binalax05@yahoo.fr
* Correspondence: kankan@hhu.edu.cn; Tel.: +86-151-5186-2390

Abstract: Due to the existence of an inlet elbow, transmission shaft, and other structural components, the inflow of axial-flow pumps as turbines (PATs) becomes non-uniform, resulting in the complexity of internal flow and adverse effects such as structural vibration. In this paper, numerical methods were employed to explore the non-uniform inflow effects on impeller forces and internal flow field characteristics within an axial-flow PAT. The study results indicated that non-uniform inflow caused uneven pressure distribution inside the impeller, which leads to an imbalance in radial forces and offsetting the center of radial forces. With an increasing flow rate, the asymmetry of radial forces as well as the amplitude of their fluctuations increased. Non-uniform inflow was found to induce unstable flow structures inside the impeller, leading to low-frequency, high-amplitude pressure fluctuations near the hub. Using the enstrophy transport equation, it was shown that the relative vortex generation term played a major part in the spatiotemporal evolution of vortices, with minimal viscous effects.

Keywords: axial-flow pump; pump as turbine; impeller force; non-uniform inflow; axial force fluctuations

1. Introduction

Pumps are the most typical and widely used piece of hydraulic machinery with an extensive range of applications in fields such as drainage and irrigation, water transfer, industry, and water environment [1,2]. As a vane-type hydraulic machinery, in addition to its basic functions, the pump also has the ability to operate in reverse to generate electricity. Comparing different types of pumps, axial-flow pumps, owing to their geometric structure, have excellent flow passage characteristics and can generate more electrical energy under the same head and geometry [3]. According to the existing literature, in small-scale hydropower stations, it is feasible for reverse-run axial-flow pumps to replace conventional hydraulic turbines for hydroelectricity generation [4–6]. Axial-flow pumps working as turbines (pump as turbine, PAT) not only generate clean energy but also generate considerable economic benefits [5]. Compared with traditional turbine units, PATs have a simple structure, low cost, and easy maintenance, making them highly suitable for facilitating the sustainable use of water resources in remote rural regions [7,8]. However, the design and manufacture of axial-flow pumps usually only consider the performance under conventional pump conditions, rather than reverse operating conditions [9]. Additionally, considering the existence of an inlet elbow, transmission shaft, and other structural components, the inflow conditions during the reverse operation of axial-flow pumps are poor,

resulting in reduced uniformity in fluid distribution within the impeller's front section. The formation of non-uniform inflow induces an imbalance in impeller forces, increasing the complexity of internal flow inside the PAT [10–12]. This leads to poor stability of the axial PAT with lower efficiency, vibrations, and a limited high-efficiency range [13,14], presenting a substantial menace to the secure and stable operation of hydraulic machinery. Consequently, it becomes significant to explore the non-uniform inflow effects on impeller forces within axial-flow PATs.

Currently, extensive studies have been carried out to investigate the issue of impeller forces within hydraulic machines. Zhang et al. [15] used numerical methods to study the blade arrangement effects on impeller radial forces within a centrifugal pump. The findings showed that the radial force vector diagram of the symmetric impeller exhibited a hexagonal shape, whereas it was close to circular for the staggered impeller. The staggered blade arrangement could evidently decrease the radial force fluctuation. In a study conducted by Tan et al. [16], a comparative analysis was performed on the radial forces of a centrifugal pump with varying guide vane outlet angles. The findings demonstrated that a decreasing outlet angle led to improved flow uniformity within the pump, resulting in a significant reduction in radial force fluctuations. Zhu et al. [17] numerically simulated a reversible pump turbine to investigate the impact of leading-edge cavitation on the impeller axial force operating under pumping conditions and found the axial force exhibited a pattern of initial increase followed by a rapid decrease with the progression from no cavitation to critical cavitation. The cavitation that occurred in impeller blades affected the load distribution, thus causing changes in the axial force. Jin et al. [18] investigated the characteristics of impeller axial force within the varying-speed centrifugal pump, where it was revealed that the axial force evolution demonstrated a comparable trend to that of the pump head. Under the variable speed conditions, when the rotational speed changed from high to low, the axial force direction exhibited a shift from a positive to a negative orientation. Qian et al. [19], with the aim to optimize the impeller blade parameters in multistage pumps, established a multivariate regression model. Optimum parameter combinations were obtained, taking into consideration the pump performance and axial force.

In addition, recent years have again seen many more scholars discussing the non-uniform inflow effects on hydraulic machinery. It was revealed that non-uniform inflow resulted in increased impeller axial force fluctuations, pressure pulsation levels, and hydraulic losses, potentially contributing to a subsequent reduction in pump head and efficiency [20–22]. Meng et al. [10] analyzed the impact of non-uniform inflow within a vertical axial-flow pump and found that the increasing inflow non-uniformity would increase the stress of the impeller, consequently raising the risk of failure due to fatigue. In a study conducted by Wang et al. [23,24], research results showed that the reduced uniformity of inflow resulted in a decrease in pump head and operational efficiency, which made the flow inside the impeller more complex and impeller forces more unbalanced. Zhang et al. [25] investigated the non-uniform inflow effects on the flow field and impeller load within the axial-flow pump. The non-uniformity of pump inflow was observed to considerably alter the velocity distribution of the impeller inlet zone, causing the variation in the angle of attack, and affecting the impeller load distribution. Luo et al. [26] performed numerical simulations on a water-jet pump to explore the energy losses and pressure fluctuation characteristics caused by non-uniform inflow, finding that the non-uniform inflow resulted in intense pressure pulsation near the channel inlet zone and within the impeller and diffuser flow fields, causing significant energy losses.

From the above-discussed literature, it is evident that recent research on the impeller force characteristics within hydraulic pumps primarily focused on the pump's conventional mode of operations for mixed and axial-flow pumps. On the other hand, published studies on the same aspect, but now considering the pump's reverse mode of operations are, to the authors' best knowledge, still limited. This hinders PAT technology's fast-paced and widespread adoption as a cost-effective alternative for small-scale hydroelectric energy generation. Consequently, this study aimed to investigate impeller forces, pressure pulsation,

and flow characteristics inside the axial-flow PAT under non-uniform inflow conditions. This is performed in the hope of providing a theoretical foundation for guaranteeing hydraulic stability within axial-flow PATs.

The rest of this paper is organized as follows: Section 2 introduces the geometric model and numerical methods. Section 3 presents the obtained results, including a comprehensive discussion on the effects of non-uniform inflow on impeller forces within an axial-flow PAT. Finally, Section 4 provides this study's drawn concluding remarks.

2. Flow Geometry and Modeling

2.1. Geometric Model

The subject of this study is an axial-flow pump model, with the computational domain comprising four sections: the inlet pipe, guide vane, impeller, and outlet pipe, which are defined in reverse operating conditions, as illustrated in Figure 1. The fundamental design parameters of the pump are presented in Table 1.
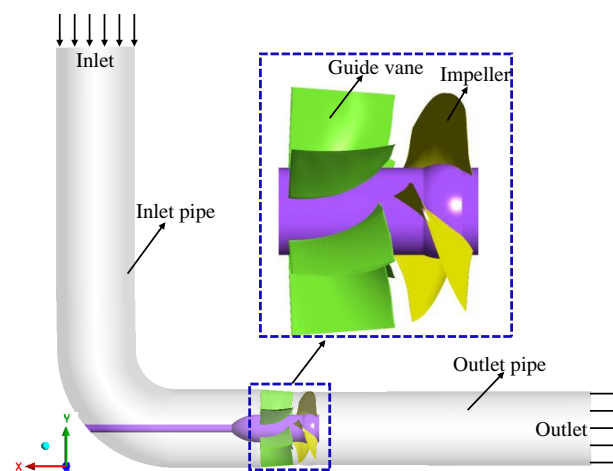

Figure 1. Geometric model of the PAT.

Table 1. Design parameters of the PAT.

Parameters	Value
Design flow rate Q (L/s)	396.94
Design head H (m)	4.91
Rotational speed n (r/min)	1450
Number of impeller blades	3
Number of guide vane blades	6
Impeller diameter D (mm)	299.2

2.2. Governing Equations

The continuity and momentum equations are as follows:

$$\frac{\partial u_i}{\partial x_i} = 0 \tag{1}$$

$$\frac{\partial(\rho u_i)}{\partial t} + \frac{\partial(\rho u_i u_j)}{\partial x_j} = -\frac{\partial p}{\partial x_i} + \frac{\partial}{\partial x_j}(\mu \frac{\partial u_i}{\partial x_j}) + \frac{\partial \tau_{ij}}{\partial x_j} \tag{2}$$

where ρ denotes the density; t represents the time; x_i and x_j denote the Cartesian coordinate components in the i and j directions, respectively; u_i and u_j denote the corresponding components of the velocity; p represents the pressure; μ represents the dynamic viscosity; and τ_{ij} represents the Reynolds stress [27].

2.3. Turbulence Model

The turbulence model employed in this study is the SST k-ω model, which treats different flow regions differently through a blending function, allowing for accurate simulation of separation vortices induced by various pressure gradients [28,29].

The k and ω equations are written as follows:

$$\frac{\partial(\rho k)}{\partial t} + \frac{\partial}{\partial x_j}(\rho u_j k) = \frac{\partial}{\partial x_j}\left[\left(\mu + \frac{\mu_t}{\sigma_k}\right)\frac{\partial k}{\partial x_j}\right] + P_k - \beta^* \rho k \omega \qquad (3)$$

$$\frac{\partial(\rho \omega)}{\partial t} + \frac{\partial}{\partial x_j}(\rho u_j \omega) = \frac{\partial}{\partial x_j}\left[\left(\mu + \frac{\mu_t}{\sigma_\omega}\right)\frac{\partial \omega}{\partial x_j}\right] + \alpha\frac{\omega}{k}P_k - \beta\rho\omega^2 + 2\rho(1 - F_1)\frac{\sigma_{\omega 2}}{\omega}\frac{\partial k}{\partial x_j}\frac{\partial \omega}{\partial x_j} \quad (4)$$

$$\mu_t = \frac{a_1 k \rho}{\max(a_1\omega, SF_2)} \qquad (5)$$

F_1 and F_2 are calculated as follows:

$$F_1 = \tanh\left\{\left\{\min\left[\max\left(\frac{\sqrt{k}}{\beta^*\omega y}, \frac{500\mu}{\rho y^2\omega}\right), \frac{4\rho\sigma_{\omega 2}k}{CD_{k\omega}y^2}\right]\right\}^4\right\} \qquad (6)$$

$$F_2 = \tanh\left\{\left[\max\left(\frac{2\sqrt{k}}{\beta^*\omega y}, \frac{500\mu}{\rho y^2\omega}\right)\right]^2\right\} \qquad (7)$$

where k represents the turbulent kinetic energy, ω represents the turbulent frequency, P_k denotes the production of turbulence kinetic energy, S denotes the mean rate of the strain tensor, and y denotes the distance from the wall. The associated constants are as follows: $a_1 = 0.31$, $\beta^* = 0.09$, $\beta = 0.075$, $\sigma_k = 1.176$, $\sigma_\omega = 2$, and $\sigma_{\omega 2} = 0.856$ [30,31].

2.4. Mesh Generation

Utilizing ICEM-CFD 19.2 software, the entire computational domain has been divided into a structured hexahedral mesh. The impeller region is structured using a J-type topology, while the guide vane region utilizes an H-type topology. The near-wall region is refined using additional mesh refinement techniques. To verify the mesh independence, the grid convergence index (GCI) [32] is employed to assess the numerical errors introduced by the mesh scheme. Three sets of grids are designed from coarse to fine to verify the grids' independence. The efficiency and torque are chosen as the parameters for grid convergence analysis and their calculated discrete error parameter values are shown in Table 2. The GCI results are less than 1%, which satisfies the mesh convergence criteria [33,34]. Considering both computational accuracy and efficient resource utilization, a total mesh count of 9.1 million is determined. Figure 2 presents the local refinement mesh of the impeller blade.
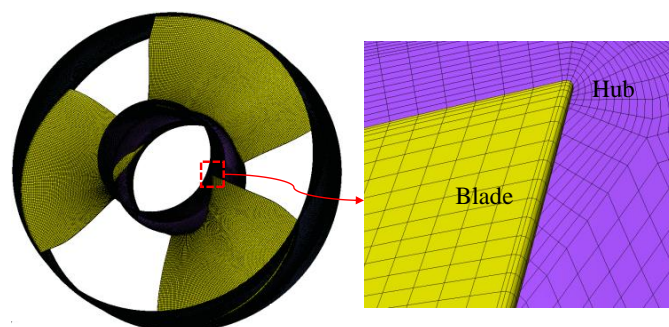

Figure 2. Local refinement mesh of the impeller blade.

Table 2. Mesh independence study.

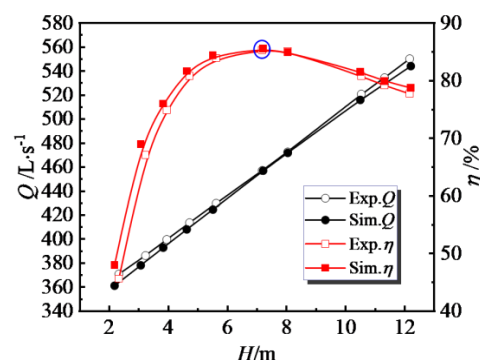| Parameter	$\varphi = \eta$ (%)	$\varphi = T$ (N·m)
N_1		19,886,600
N_2		9,092,056
N_3		4,092,919
Mesh refinement factor r_{21}		1.30
Mesh refinement factor r_{32}		1.30
Numerical value φ_1	85.70150254	182.42646
Numerical value φ_2	85.69843456	182.09172
Numerical value φ_3	85.61868887	181.81577
Extrapolated value φ_{ext}	85.3617362	181.6503352
Relative error e_a	0.09%	0.15%
Extrapolated error e_{ext}	0.3%	0.09%
Grid convergence index GCI_{fine}	0.38%	0.11%

2.5. Numerical Details

In this paper, spatial discretization is carried out by adopting the finite volume method, and the SIMPLEC algorithm is applied to achieve a coupled pressure-velocity solution. The inlet and outlet boundary conditions are set as pressure inlet and pressure outlet, respectively. The impeller region is defined as a rotating zone, and other regions are considered stationary. For the dynamic-static interface, steady-state simulations adopt the Frozen Rotor approach, while transient simulations are set as the Transient Rotor-Stator. For transient simulations, the initial data are obtained from the steady-state simulation results, and the simulation progresses with the time step size of approximately 1.15×10^{-4} s, corresponding to a $1°$ rotation of the impeller per time step. The first-order implicit scheme is used to discretize time terms, and the second-order upwind scheme is used for spatial discretization. All wall surfaces are assumed to be non-slip walls, and numerical simulations are considered to have converged when the residual is below 10^{-5}.

3. Results and Analysis

3.1. CFD Validation

Figure 3 represents the comparison of the external characteristics of the axial-flow PAT attained numerically and experimentally. (The experimental data are provided by Jiangsu Aerospace Hydraulic Equipment Co., Ltd., Gaoyou, China) With an increasing flow rate, the efficiency initially rises and then gradually declines. When deviating from the best efficiency point (BEP) indicated by the outlined annotation in Figure 3, the efficiency gradually lowers, attaining the lowest value under the smallest flow condition. From the graph, it is obvious that the simulation results align well with the experimental data, particularly in the optimum condition. The level of numerical error as compared to the experimental data is negligible, indicating the high precision of the utilized numerical scheme and, thus, the trustworthiness of related findings.

Figure 3. Comparison between the experimental and simulation results.

3.2. Analysis of the Impeller Force

Figure 4 illustrates the pressure distribution at the guide vane inlet for three flow conditions (0.8 Q_{BEP}, 1.0 Q_{BEP}, and 1.2 Q_{BEP}). From this graph, the pressure distribution at the guide vane inlet is non-uniform in the radial Y and Z directions. There is a noticeable low-pressure region in the +Y direction, the distribution of which is asymmetric in the Z direction. Under low-flow conditions, the low-pressure values in the +Z region are smaller compared to the −Z region, while the opposite is observed under the optimum and high-flow-rate conditions. This non-uniformity in the fluid distribution at the guide vane inlet is caused by the presence of components such as the inlet elbow and the transmission shaft, which results in an asymmetric pressure distribution at the guide vane inlet in the radial direction.
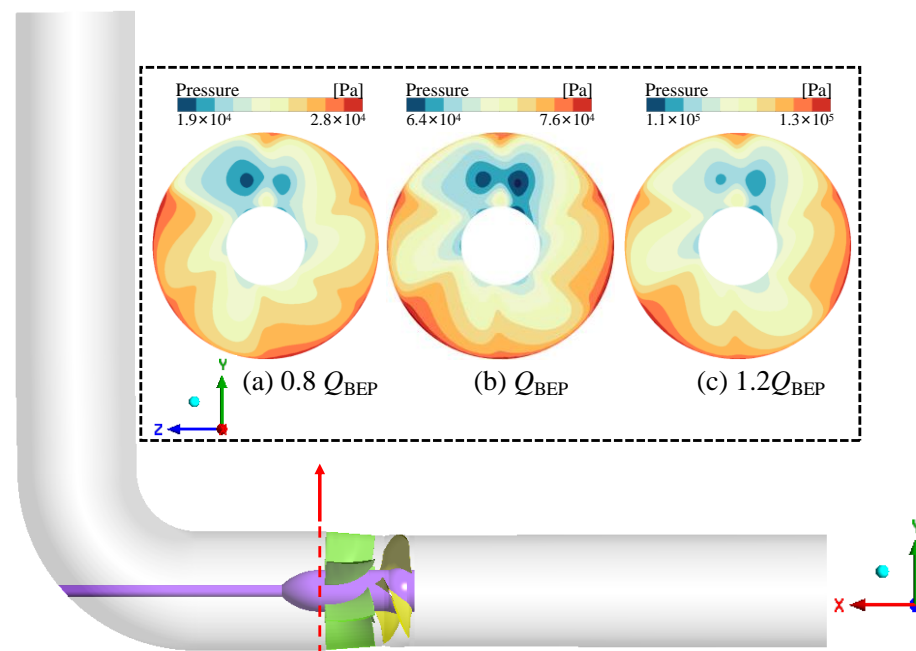

Figure 4. Pressure distribution at the guide vane inlet.

Figure 5 presents the pressure distribution on the pressure surface of impeller blades for one blade period ($T/3$), where T is the impeller rotation period. At low-flow conditions, a localized low-pressure region is observed in close proximity to the blade leading edge (LE). In the flow direction, there is a gradual increase in pressure. However, at optimum and high-flow conditions, a localized high-pressure region is located near the blade LE, and there is a gradual decrease in the flow direction. In this graph, it can be noticed that the pressure distribution on impeller blades exhibits non-uniformity in the radial direction. As the forces on the impeller blades are integrated from the pressure, there is an imbalance in the radial forces.

By conducting transient simulations of the PAT under three flow rate conditions, the three-dimensional impeller forces are obtained, as shown in Figure 6. The transient simulations are carried out for a total of 20 periods, and the analysis of impeller forces is performed during the last period. When axial-flow pumps operate in reverse power generation, the main flow direction is −X, resulting in axial force Fx remaining negative. The projection on the YZ plane represents the radial forces trajectory, with most of the radial forces located in the −Z and +Y directions. The magnitudes of axial and radial forces differ in the orders of magnitude, resulting in irregular-shaped force trajectories in the XY and XZ planes. Evidently, the shape of the radial force trajectory deviates from circular or elliptical and exhibits asymmetry. With the increasing flow rate, the range of radial force trajectories expands, and the degree of asymmetry in the radial forces increases. This may be due to

the fact that the impeller inflow reduces the uniformity of the pressure distribution in the flow field around the impeller, which leads to an imbalance in the radial forces.
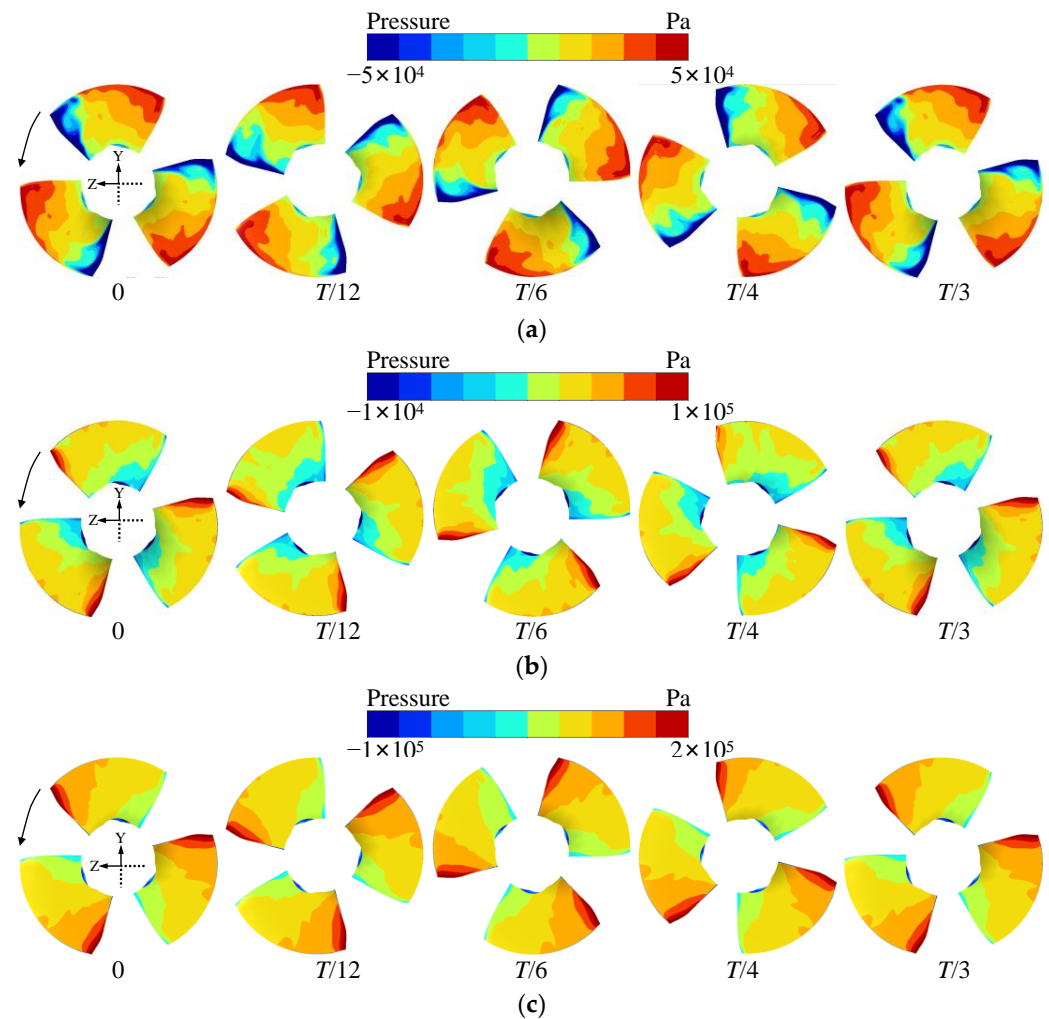

Figure 5. Pressure distribution on the impeller blade: (**a**) 0.8 Q_{BEP}; (**b**) Q_{BEP}; and (**c**) 1.2 Q_{BEP}.
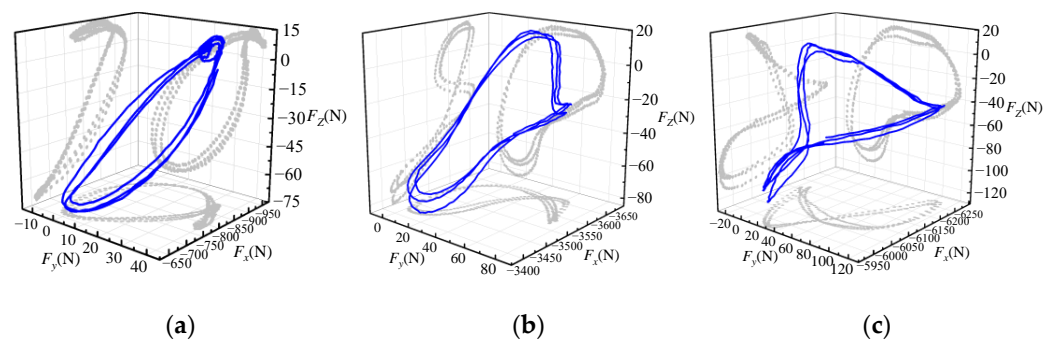

Figure 6. Three-dimensional forces distribution characteristics of impeller: (**a**) 0.8 Q_{BEP}; (**b**) Q_{BEP}; and (**c**) 1.2 Q_{BEP}.

Figure 7 illustrates the variation laws of axial force and total radial force of the impeller with time under three flow rate conditions, where t_n represents the impeller rotation period. The total radial force is written in Equation (9). In Figure 7b, the trajectory of the total radial force at the initial and final moments approximately forms a closed loop in one period, indicating that the impeller force has become relatively stable. At different operating conditions, the variation in impeller force is approximately the same. The impeller forces in

the radial direction and axial direction show periodic changes within one impeller rotation period, with the peaks and valleys roughly occurring at the same moments. With an increasing flow rate, both the axial force and radial force exhibit a gradual increment.

$$F_r = \sqrt{F_y{}^2 + F_z{}^2} \tag{8}$$

In this paper, the force coefficient C_F is used to reflect the pulsation amplitude, which is defined as follows:

$$C_F = \frac{(F_i - F_{ave})}{0.5\rho u_{tip}{}^2 A_2} \tag{9}$$

where F_i represents the transient force, F_{ave} represents the average force over a time period, A_2 denotes the area of the impeller outlet, and u_{tip} is the circumferential velocity of the impeller blade tip [35].
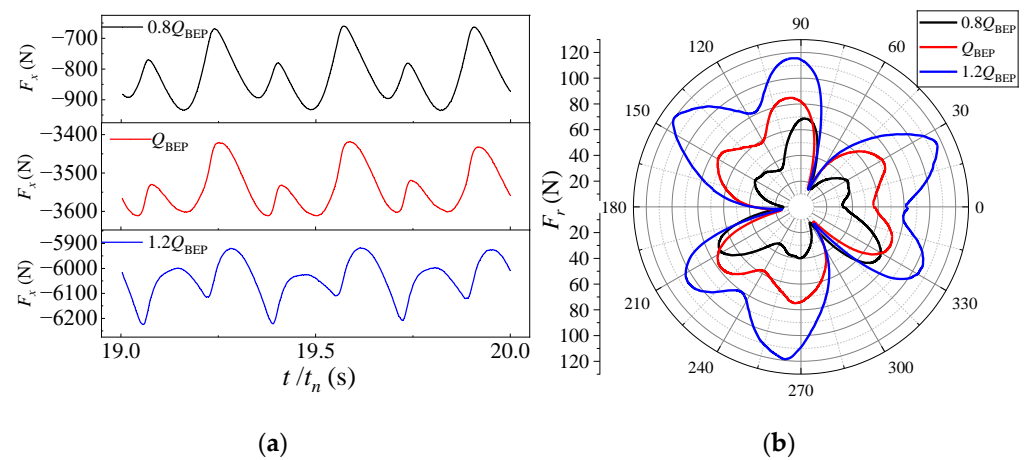

(**a**)　　　　　　　　　　　(**b**)

Figure 7. The variation laws of axial force and total radial force of the impeller with time under three flow rate conditions: (**a**) axial force F_x; (**b**) total radial force F_r.

Figure 8 displays the pulsation characteristics of the axial and radial forces of the impeller under three flow rate conditions, where f_n is the impeller rotation frequency. When the PAT operates away from the optimum condition, the axial force exhibits a larger fluctuation amplitude, which is 1.5 times that of the optimum condition. Under high-flow conditions, the radial force displays the most intense fluctuation amplitude, resulting in the strongest vibrations in the PAT. With the decreasing flow rate, the fluctuation amplitude of radial forces gradually reduces. When subjected to the same flow conditions, the fluctuation amplitude of the radial force in the Y direction is observed to be lesser in comparison to the Z direction. Furthermore, under low-flow and optimum conditions, the difference in the amplitude of radial force fluctuations between the two directions is more pronounced. The axial force exhibits the most intense fluctuation at $6f_n$, while the dominant frequency of radial forces is $3f_n$.
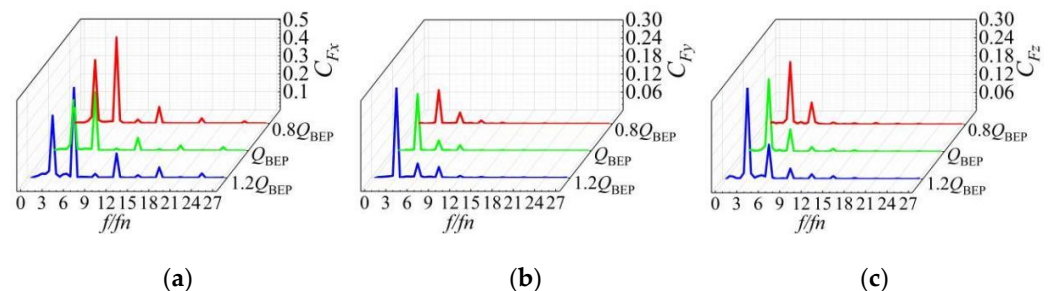

(**a**)　　　　　　　　　　(**b**)　　　　　　　　　　(**c**)

Figure 8. The pulsation characteristics of the axial and radial forces of the impeller under three flow rate conditions; (**a**) axial force C_{Fx}; (**b**) radial force C_{Fy}; and (**c**) radial force C_{Fz}.

3.3. Pressure Pulsation of Impeller Blades

To study the flow characteristics inside the PAT, the frequency domain characteristics of pressure values at various monitoring points on impeller blades were analyzed employing the Fast Fourier Transform method. Figure 9 presents the schematic diagram depicting the locations of pressure monitoring points on impeller blades. Figure 10 illustrates the frequency domain of pressure fluctuations at various positions on the pressure surface. In this figure, the vertical coordinate represents the pressure coefficient, which is calculated as follows:

$$C_p = \frac{(P_i - P_{\text{ave}})}{0.5\rho u_{tip}{}^2} \tag{10}$$

In this formula, P_i stands for the transient pressure and P_{ave} is the average pressure over a time period [36].

When PAT operation deviates from the optimum condition, the pressure pulsation amplitude close to the blade LE along the flow direction becomes the largest. This is due to the fact that, when deviating from the optimum condition, the non-uniformity of impeller inflow increases, leading to intense pressure fluctuations near the blade LE. Nevertheless, pressure fluctuations close to the blade trailing edge (TE) under optimum conditions are the most intense, indicating that under these conditions, the impeller inflow has relatively favorable inflow conditions, with an unstable flow structure occurring in the blade TE region. Under three flow rate conditions, pressure fluctuations on the pressure surface are most severe near the hub, gradually decreasing in amplitude from the impeller hub towards the shroud. As the flow rate increases, pressure fluctuations become more intense. For all studied flow conditions, the dominant frequency of pressure fluctuations is $1f_n$. This is due to the setting of the rotor-stator interface in CFX simulations which causes the monitoring points on the blades to rotate with the impeller. Relatively, the inlet elbow seems to be rotating relative to the monitoring points.

The frequency domain characteristics of pressure pulsation on blade suction surfaces are presented in Figure 11. Observing closely, at low-flow conditions, pressure pulsations are more severe near the impeller shroud on the suction surface. Along the radial direction, pressure pulsation amplitudes are found to gradually increase from the impeller hub towards the shroud. Under optimum and high-flow conditions, the maximum amplitude of pressure pulsations is located near the hub on the suction surface, from where the fluctuation amplitude decreases toward the shroud, along the radial direction. Along the flow direction, there is a gradual reduction in the amplitude of fluctuations from the blade LE toward the TE zone. The pressure pulsation amplitude of the dominant frequency is found to grow larger as the flow rate increases. For all studied flow conditions, the maximum pressure fluctuation amplitude on the suction surface occurs at $1f_n$. According to the above analysis, for an axial-flow PAT, the presence of an inlet elbow gives rise to non-uniform inflow conditions, leading to complex pressure fluctuations on the blade. These fluctuations further contribute to the instability of the impeller force.
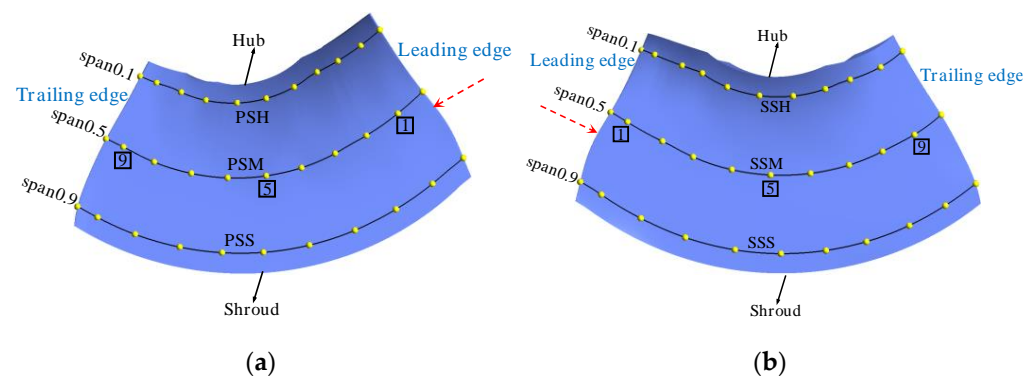

(**a**)   (**b**)

Figure 9. Schematic diagram of pressure pulsation monitoring points of impeller blade; (**a**) pressure surface; (**b**) suction surface.
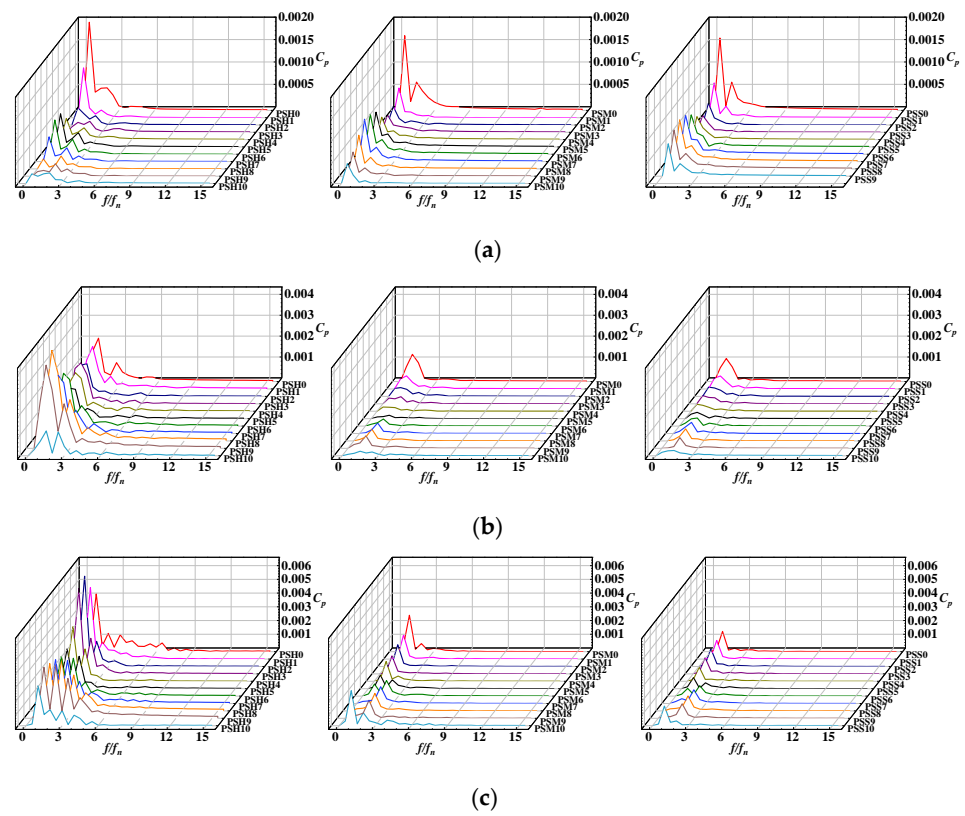
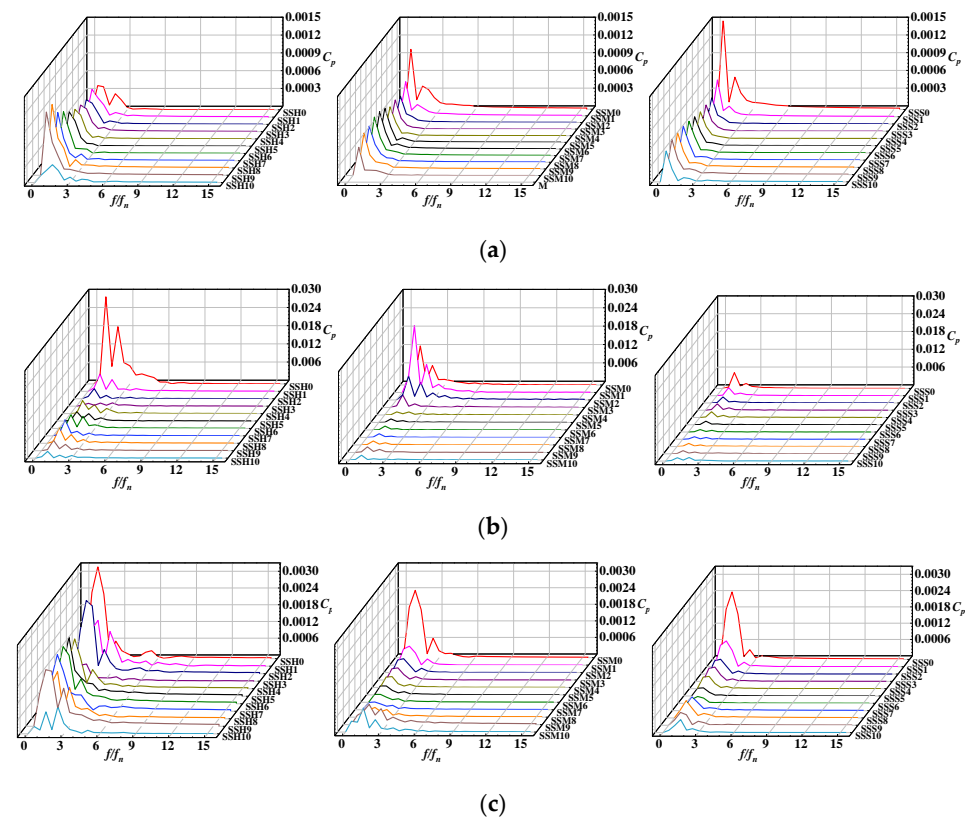**Figure 10.** Frequency domain of pressure fluctuation on pressure surface: (**a**) 0.8 Q_{BEP}; (**b**) Q_{BEP}; and (**c**) 1.2 Q_{BEP}.

Figure 11. Frequency domain of pressure fluctuation on the suction surface: (**a**) 0.8 Q_{BEP}; (**b**) Q_{BEP}; and (**c**) 1.2 Q_{BEP}.

3.4. Analysis of the Flow Field Inside the Impeller

From the above analysis, it can be obtained that there are unstable flow structures inside the impeller that affect the uniformity of pressure distribution and the balance of radial forces; thus, the flow field of the impeller section is analyzed. The flow field close to the impeller hub side (span = 0.1 in the spanwise direction) is selected for further analysis.

Figure 12 shows the enstrophy distribution on a blade-to-blade surface close to the hub under different flow conditions. The formula for enstrophy is defined as $\omega^2/2$, where ω is the vorticity [37]. By comparing the enstrophy distribution in the Z direction near the impeller hub when t = 0, it is evident that in the $-Z$ direction, there is a region of high enstrophy that persists, surpassing the enstrophy value observed in the +Z direction, indicating that the strength of the vortex flow which exists in the $-Z$ direction is more intense. As the flow rate increases, the greater the difference in entropy values between the +Z and $-Z$ direction regions. The unstable vortex structure leads to low-frequency, high-amplitude pressure pulsations, which further worsen the imbalance of radial forces on the impeller. For different flow conditions, the enstrophy zone close to the blade TE is found to gradually increase with time, and the vortex intensity increases with an increasing flow rate.

To further investigate the generation and development of vortices, the vortex flow is analyzed using the enstrophy transport equation [38,39], which is defined as follows:

$$\frac{\partial(\overline{\omega}_i\overline{\omega}_i/2)}{\partial t} = G_\omega + R_\omega + C_\omega + B_\omega + V_\omega \tag{11}$$
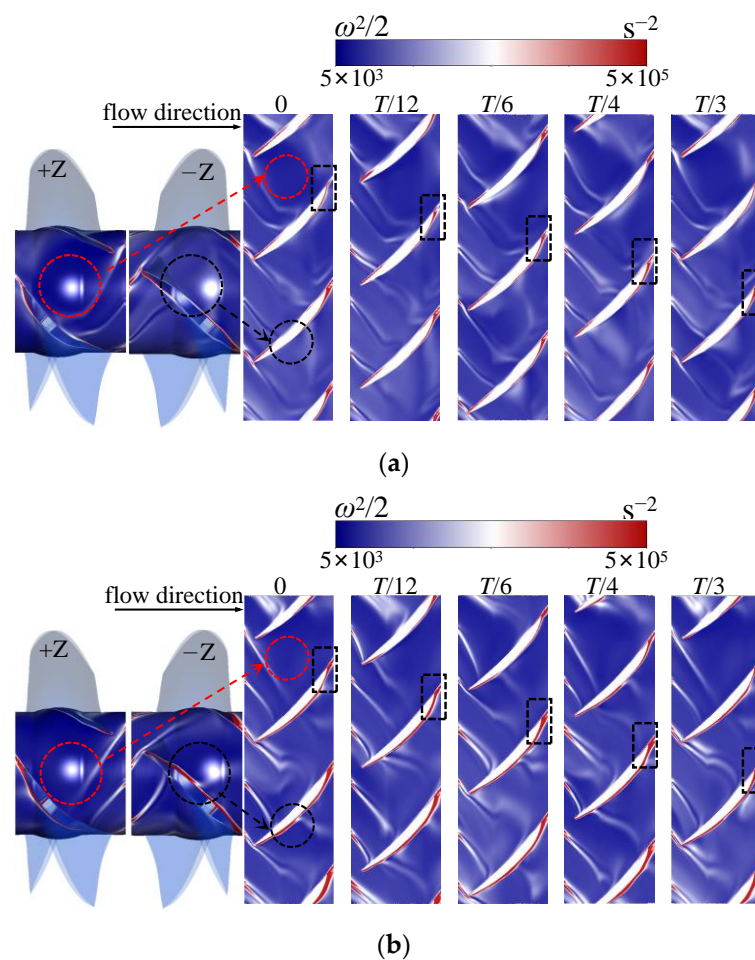

(a)

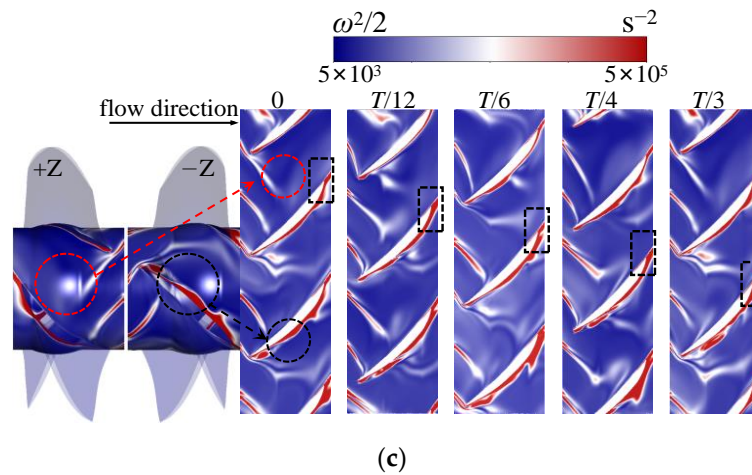(b)

Figure 12. *Cont.*

(c)

Figure 12. Enstrophy distribution on the blade-to-blade surface: (**a**) 0.8 Q_{BEP}; (**b**) Q_{BEP}; and (**c**) 1.2 Q_{BEP}.

Equation (11) represents the enstrophy transport equation, where each term on the right is defined as follows:

$$G_\omega = \overline{\omega}_i \overline{S}_{ij} \overline{\omega}_j - \overline{u}_j \frac{\partial(\overline{\omega}_i \overline{\omega}_i / 2)}{\partial x_j}, \tag{12}$$

$$R_\omega = \nu_t \left(\frac{\partial^2 \overline{\omega}_i}{\partial x_j \partial x_j} \overline{\omega}_i + \frac{\partial^2 \overline{\omega}_j}{\partial x_j \partial x_i} \overline{\omega}_i \right) - \frac{2}{3} \varepsilon_{ijk} \frac{\partial^2 k}{\partial x_i \partial x_j} \overline{\omega}_k, \tag{13}$$

$$C_\omega = -2 \left(\frac{\partial(c_i \overline{u}_j)}{\partial x_j} \overline{\omega}_i - \frac{\partial(c_i \overline{u}_j)}{\partial x_i} \overline{\omega}_j \right), \tag{14}$$

$$B_\omega = \frac{1}{\rho^2} \varepsilon_{ijk} \overline{\omega}_i \frac{\partial \rho}{\partial x_j} \frac{\partial p}{\partial x_k}, \tag{15}$$

$$V_\omega = \nu \frac{\partial^2 \overline{\omega}_i}{\partial x_j \partial x_j} \overline{\omega}_i. \tag{16}$$

where $\overline{\omega}_i$ represents the Reynolds-averaged vorticity; $\overline{S}_{ij}$ is the mean strain tensor; ε_{ijk} is the permutation symbol; c_i is the angular velocity; $\overline{u}_j$ is the Reynolds-averaged velocity; ν represents the kinematic viscosity; ν_t represents the eddy viscosity; G_ω is the relative vortex generation term, indicating the stretching and bending of vorticity owing to velocity gradients; R_ω represents the Reynolds stress dissipation term; C_ω represents the Coriolis force term; B_ω is a baroclinic torque term, representing the variation in vorticity because of the non-parallelism of pressure and density gradients, which is neglected due to the fluid incompressibility; and V_ω is a viscous term, representing the vorticity variation caused by the fluid viscosity.

Figures 13–15 show the distribution of each term of the enstrophy transport equation on the considered blade-to-blade surface inside the impeller for all studied flow conditions. The crucial role of the relative vortex generation term G_ω in the evolution and development of vortices is clearly evident, followed by the Reynolds stress dissipation term R_ω and Coriolis force term C_ω, while the viscosity term V_ω has the least influence. Influenced by the impeller's inflow conditions, there are high-value regions of enstrophy near the blade LE, resulting in sustained pressure fluctuations at the same zone and vicinities. With an increasing flow rate, the regions of enstrophy near the blade LE gradually extend to adjacent blades, and the values of enstrophy gradually increase. Meanwhile, the blade TE region also exhibits a high value for each term in the entropy transport equation, and the region expands gradually with time.
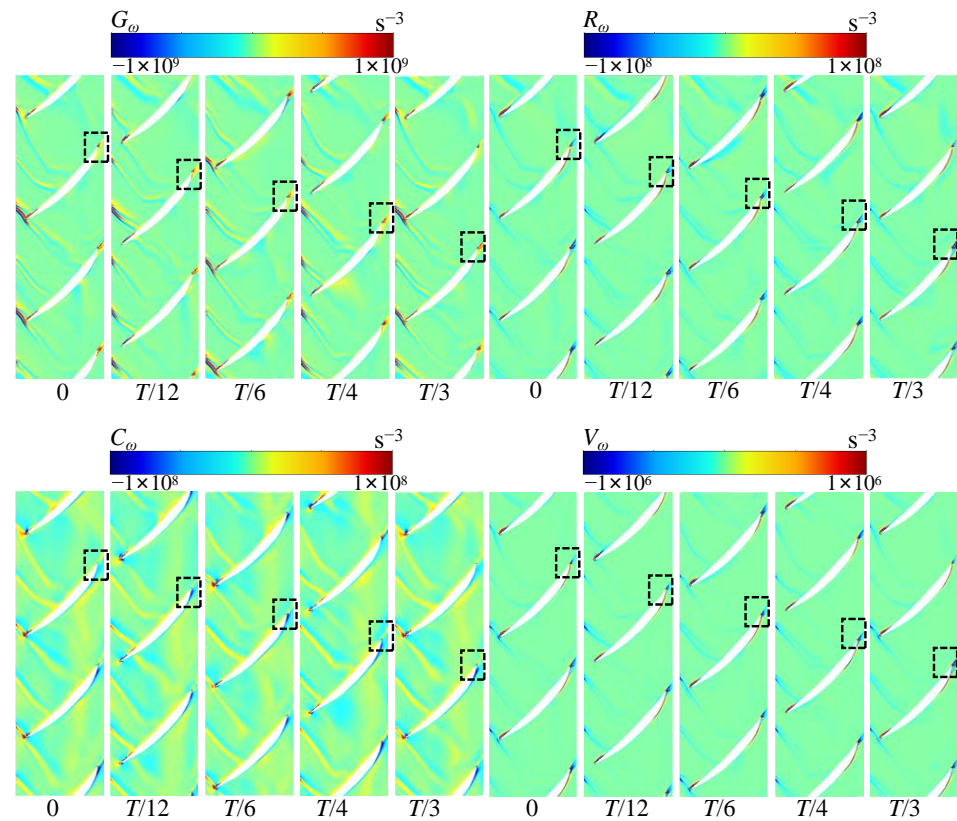
Figure 13. Distribution of each term of the enstrophy transport equation on the blade-to-blade surface under $0.8Q_{BEP}$.
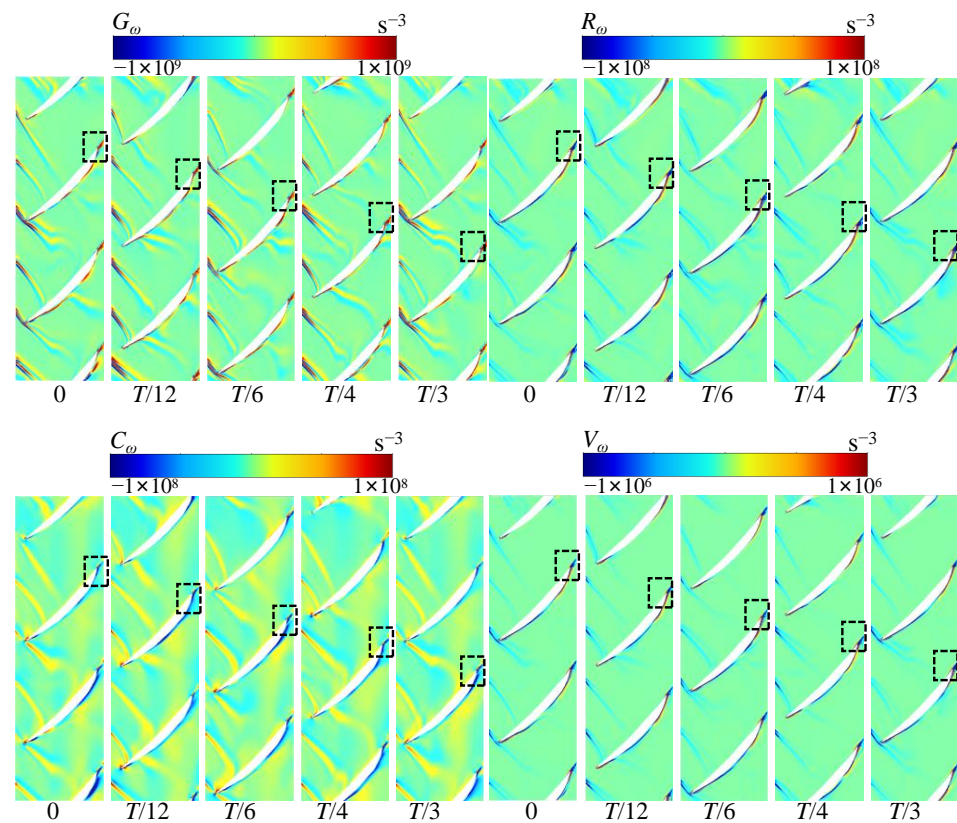

Figure 14. Distribution of each term of the enstrophy transport equation on the blade-to-blade surface under Q_{BEP}.
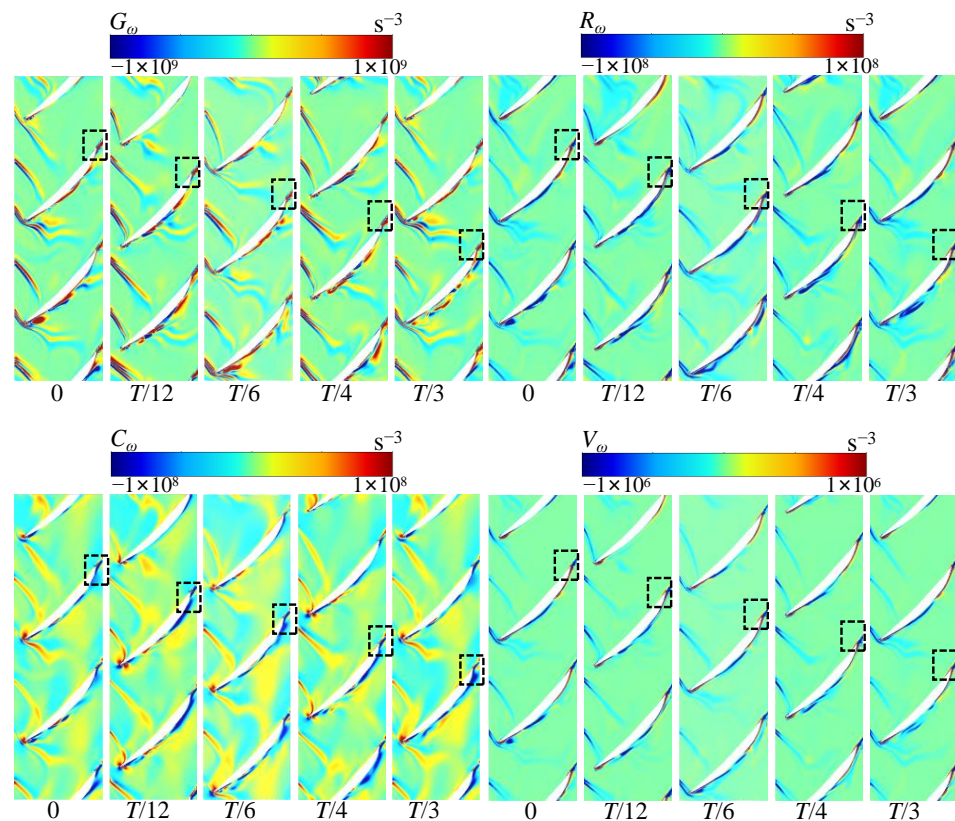
Figure 15. Distribution of each term of the enstrophy transport equation on the blade-to-blade surface under $1.2Q_{BEP}$.

4. Conclusions

In this study, an axial-flow pump as a turbine was numerically simulated for different flow conditions near its BEP. This study's main goal was to analyze the non-uniform inflow effects on impeller forces within axial-flow PATs. The conclusions were as follows:

(1) The presence of the inlet elbow and transmission shaft reduces the uniformity of the fluid distribution in front of the guide vane in the axial-flow PAT, and the impact of inflow non-uniformity can still be felt farther downstream within the impeller flow field. This influences the pressure distribution within the impeller, leading to an imbalance of impeller forces and a subsequent offset in the center of radial forces. With a gradual increase in PAT influx, the amplitudes of impeller radial force fluctuations are found to correspondently increase.

(2) The inflow non-uniformity caused by the inlet elbow structure of the PAT is found to be the main factor influencing the pressure fluctuations on impeller blades. Under three tested flow conditions, pressure fluctuations are more severe near the impeller hub side, the fluctuation amplitude of which gradually decreases from the hub towards the shroud. When deviating from the optimum condition, the amplitude of pressure fluctuations exhibits its highest magnitude in close proximity to the blade leading edge along the flow direction. Moreover, as the flow rate increases, pressure fluctuations on the blade surface become more intense.

(3) Non-uniform inflow is found to induce unstable flow structures such as vortices inside the impeller, leading to low-frequency, high-amplitude pressure fluctuations near the hub. The development process of the vortices is analyzed using the enstrophy transport equation, indicating that the relative vortex generation term near the hub is obviously greater than the other three terms and consistently dominates. The Coriolis force term exhibits a greater effect on the evolution process of vortices compared to the Reynolds stress dissipation term, and the viscosity term has the least influence.

References

1. Hu, J.; Su, W.; Li, K.; Wu, K.; Xue, L.; He, G. Transient hydrodynamic behavior of a pump as turbine with varying rotating speed. *Energies* **2023**, *16*, 2071. [CrossRef]
2. Kan, K.; Yang, Z.; Lyu, P.; Zheng, Y.; Shen, L. Numerical study of turbulent flow past a rotating axial-flow pump based on a level-set immersed boundary method. *Renew. Energy* **2021**, *168*, 960–971. [CrossRef]
3. Qin, D.; Wu, X.; Zhang, J.; Wang, X.; Yan, N. Hydraulic optimisation design of axial flow pump based on blade velocity distribution. *Int. J. Hydromechatron.* **2023**, *6*, 311–324. [CrossRef]
4. Qian, Z.; Wang, F.; Guo, Z.; Lu, J. Performance evaluation of an axial-flow pump with adjustable guide vanes in turbine mode. *Renew. Energy* **2016**, *99*, 1146–1152. [CrossRef]
5. Zhang, X.; Tang, F.; Jiang, Y. Experimental and numerical study of reverse power generation in coastal axial flow pump system using coastal water. *Ocean Eng.* **2023**, *271*, 113805. [CrossRef]
6. Castorino, G.A.M.; Manservigi, L.; Barbarelli, S.; Losi, E.; Venturini, M. Development and validation of a comprehensive methodology for predicting PAT performance curves. *Energy* **2023**, *274*, 127366. [CrossRef]
7. Liu, M.; Tan, L.; Cao, S. Theoretical model of energy performance prediction and BEP determination for centrifugal pump as turbine. *Energy* **2019**, *172*, 712–732. [CrossRef]
8. Yuan, Z.; Zhang, Y.; Zhou, W.; Wang, C. Hydraulic loss analysis in a pump-turbine with special emphasis on local rigid vortex and shear. *Phys. Fluids* **2022**, *34*, 125101. [CrossRef]
9. Yu, H.; Wang, T.; Dong, Y.; Gou, Q.; Lei, L.; Liu, Y. Numerical investigation of splitter blades on the performance of a forward-curved impeller used in a pump as turbine. *Ocean Eng.* **2023**, *281*, 114721. [CrossRef]
10. Ye, H.; Xuan, X.; Wang, M.; Sun, J.; Yang, M.; Zhang, X.; Guo, L.; Sun, X. Structural Optimization of Reactor for the Enhancement of CO_2 Electrochemical Reduction Based on Gas–Liquid Mixing Flow Model. *Energy Technol.* **2024**, *12*, 2301142. [CrossRef]
11. Cao, P.; Yin, G.; Wang, Y.; Li, G.; Wu, W. Numerical analysis of double tornado-type separation vortices in centrifugal pump. *Trans. Chin. Soc. Agric. Mach.* **2016**, *47*, 22–28.
12. Chen, J.; Zhang, H.; Li, Y.; Meng, F.; Zheng, Y. Study on Inflow Distortion Mechanism and Energy Characteristics in Bidirectional Axial Flow Puming Station. *Machines* **2022**, *10*, 1014. [CrossRef]
13. Adu, D.; Zhang, J.; Jieyun, M.; Asomani, S.N.; Koranteng, M.O. Numerical investigation of transient vortices and turbulent flow behaviour in centrifugal pump operating in reverse mode as turbine. *Mater. Sci. Energy Technol.* **2019**, *2*, 356–364. [CrossRef]
14. Jemal, A.N.; Haile, M.G. Comprehensive review of pump as turbine (PAT). *Renew. Energy Sustain. Dev.* **2019**, *5*, 68. [CrossRef]
15. Zhang, Z.; Wang, F.; Yao, Z.; Leng, H.; Zhou, P. Investigation on impeller radial force for double-suction centrifugal pump with staggered blade arrangement. *IOP Conf. Ser. Mater. Sci. Eng.* **2013**, *52*, 032009. [CrossRef]
16. Tan, M.; Guo, B.; Liu, H.; Wu, X.; Wang, K. Investigation of radial force and hydraulic performance in a centrifugal pump with different guide vane outlet angle. *J. Vibroeng.* **2015**, *17*, 3247–3260.
17. Zhu, D.; Xiao, R.; Liu, W. Influence of leading-edge cavitation on impeller blade axial force in the pump mode of reversible pump-turbine. *Renew. Energy* **2021**, *163*, 939–949. [CrossRef]
18. Jin, F.; Tao, R.; Wei, Z.; Wu, Y.; Xiao, R. Investigation of the axial force on a varying-speed centrifugal pump impeller. *Proc. Inst. Mech. Eng. Part A J. Power Energy* **2022**, *236*, 714–726. [CrossRef]
19. Qian, C.; Luo, X.; Yang, C.; Wang, B. Multistage pump axial force control and hydraulic performance optimization based on response surface methodology. *J. Braz. Soc. Mech. Sci. Eng.* **2021**, *43*, 1–14. [CrossRef]
20. Van Esch, B.P.M. Performance and radial loading of a mixed-flow pump under non-uniform suction flow. *J. Fluids Eng.* **2009**, *131*, 051101. [CrossRef]
21. Long, Y.; Wang, D.; Yin, J.; Hu, Y.; Ran, H. Numerical investigation on the unsteady characteristics of reactor coolant pumps with non-uniform inflow. *Nucl. Eng. Des.* **2017**, *320*, 65–76. [CrossRef]
22. Song, Y.; Huang, S.; Xu, R.; Zhang, Z.; Yin, J.; Wang, D. Influence mechanism of the non-uniform inflow on performance of reactor coolant pump. *Ann. Nucl. Energy* **2023**, *180*, 109467. [CrossRef]

23. Wang, Y.; Wang, P.; Tan, X.; Xu, Z.; Ruan, X. Research on the non-uniform inflow characteristics of the canned nuclear coolant pump. *Ann. Nucl. Energy* **2018**, *115*, 423–429. [CrossRef]
24. Wang, Y.; Xu, Z.; Wang, P.; Wang, J.; Ruan, X. Numerical and experimental analysis on the non-uniform inflow characteristics of a reactor coolant pump with a steam generator channel head. *Eng. Appl. Comput. Fluid Mech.* **2020**, *14*, 477–490.
25. Zhang, J.; Cao, L.; Cui, J.; Ren, H.; Wang, Y.; Wu, D. Effects of non-uniform inflow on the spatial and temporal distribution of impeller excitation in axial flow pumps in water tunnels. *J. Mech. Sci. Technol.* **2023**, *37*, 5251–5262. [CrossRef]
26. Luo, X.; Ye, W.; Huang, R.; Wang, Y.; Du, T.; Huang, C. Numerical investigations of the energy performance and pressure fluctuations for a waterjet pump in a non-uniform inflow. *Renew. Energy* **2020**, *153*, 1042–1052. [CrossRef]
27. Zhang, F.; Appiah, D.; Hong, F.; Zhang, J.; Yuan, S.; Adu-Poku, K.A.; Wei, X. Energy loss evaluation in a side channel pump under different wrapping angles using entropy production method. *Int. Commun. Heat Mass Transf.* **2020**, *113*, 104526. [CrossRef]
28. Sun, X.; Xia, G.; You, W.; Jia, X.; Manickam, S.; Tao, Y.; Xuan, X. Effect of the arrangement of cavitation generation unit on the performance of an advanced rotational hydrodynamic cavitation reactor. *Ultrason. Sonochem.* **2023**, *99*, 106544. [CrossRef] [PubMed]
29. Xia, G.; You, W.; Manickam, S.; Yoon, J.Y.; Xuan, X.; Sun, X. Numerical simulation of cavitation-vortex interaction mechanism in an advanced rotational hydrodynamic cavitation reactor. *Ultrason. Sonochem.* **2024**, *105*, 106849. [CrossRef]
30. Kan, K.; Chen, H.; Zheng, Y.; Zhou, D.; Binama, M.; Dai, J. Transient characteristics during power-off process in a shaft extension tubular pump by using a suitable numerical model. *Renew. Energy* **2021**, *164*, 109–121. [CrossRef]
31. Si, Q.; He, J.; Miao, S.; Liu, J.; Asad, A.; Wang, P. Study on the energy conversion characteristics in the impeller of USSPAT based on velocity triangle space decomposition. *J. Energy Storage* **2023**, *72*, 108429. [CrossRef]
32. Meana-Fernández, A.; Fernández Oro, J.M.; Argüelles Díaz, K.M.; Galdo-Vega, M.; Velarde-Suárez, S. Application of Richardson extrapolation method to the CFD simulation of vertical-axis wind turbines and analysis of the flow field. *Eng. Appl. Comput. Fluid Mech.* **2019**, *13*, 359–376. [CrossRef]
33. Daniels, S.J.; Rahat, A.A.M.; Tabor, G.R.; Fieldsend, J.E.; Everson, R.M. Shape optimisation of the sharp-heeled Kaplan draft tube: Performance evaluation using Computational Fluid Dynamics. *Renew. Energy* **2020**, *160*, 112–126. [CrossRef]
34. Kan, K.; Zhang, Q.; Xu, Z.; Zheng, Y.; Gao, Q.; Shen, L. Energy loss mechanism due to tip leakage flow of axial flow pump as turbine under various operating conditions. *Energy* **2022**, *255*, 124532. [CrossRef]
35. Shi, W.; Chen, C.; Tan, L.; Shi, Z. Experimental study on the single blade centrifugal pump radial force. *J. Vib. Shock* **2022**, *41*, 185–192.
36. Yu, G.; Li, G.; Wang, C. Pressure pulsation characteristics of agricultural irrigation pumps under cavitation conditions. *Water* **2023**, *15*, 4250. [CrossRef]
37. Ghai, S.K.; Chakraborty, N.; Ahmed, U.; Klein, M. Enstrophy evolution during head-on wall interaction of premixed flames within turbulent boundary layers. *Phys. Fluids* **2022**, *34*, 075124. [CrossRef]
38. Kazbekov, A.; Kumashiro, K.; Steinberg, A.M. Enstrophy transport in swirl combustion. *J. Fluid Mech.* **2019**, *876*, 715–732. [CrossRef]
39. Kan, K.; Xu, Y.; Xu, H.; Feng, J.; Yang, Z. Vortex-induced energy loss of a mixed-flow waterjet pump under different operating conditions. *Acta Mech. Sin.* **2023**, *39*, 323064. [CrossRef]